Fatigue crack growth behavior of Inconel 718 produced by selective laser melting

R. Konečná
University of Žilina, Žilina, Slovakia
radomila.konecna@fstroj.uniza.sk

L. Kunz
Institute of Physics of Materials, Brno, Czech Republic
ludvik.kunz@ipm.cz

G. Nicoletto
University of Parma, Parma, Italy
gianni.nicoletto@unipr.it

A. Bača
University of Žilina, Žilina, Slovakia
adrian.baca@fstroj.uniza.sk

ABSTRACT. Additive layer manufacturing has recently gained a lot of interest due to the feasibility of producing metallic components directly from a computer-aided design file of the part. Selective laser melting, one of the main additive layer manufacturing technologies, is currently capable of producing nearly ready-to-use parts made of metallic materials. Their microstructure, however, differs substantially from that produced by conventional manufacturing. That is why a detailed study and knowledge of the relation of specific microstructure, parameters of the selective laser melting process and mechanical properties is of utmost significance.

This study reports on the investigation of the fatigue crack growth behavior in Inconel 718 superalloy produced by selective laser melting. The fatigue crack growth curve and the threshold values of the stress intensity factor for propagation of long cracks were experimentally determined on compact-tension specimens fabricated using a RENISHAW A250 system and the recommended processing parameters. The fatigue crack growth rates and the fatigue crack paths both in the threshold and in the Paris region were investigated. The crack propagation curves and the crack propagation threshold were compared with literature data describing the behavior of conventionally manufactured material. The mechanism of fatigue crack growth was discussed in terms of the specific microstructure produced by selective laser melting.

KEYWORDS. Inconel 718; selective laser melting; Microstructure; Fatigue crack growth; Fractography.

INTRODUCTION

Additive layer manufacturing (ALM) has recently gained a lot of interest due to the feasibility of producing metallic components directly from a computer-aided design file of the part. The technology has strong impact on variety of industries, e.g. automotive, shipping, and aerospace [1]. Selective laser melting (SLM), one of the main ALM technologies, is currently capable of producing nearly ready-to-use parts made of many metallic materials, including Ni-based superalloys [2].

Conventionally manufactured Inconel 718 is frequently used for high temperature applications (up to 700 °C) as jet engine and high-speed airframe parts, gas turbines, exhaust manifolds, turbochargers, etc. The microstructure of the alloy consists of a nickel-rich γ matrix, which has a face-centered cubic (fcc) lattice structure with many different precipitates. The fine grain size is sought because leads to an increase in yield and ultimate tensile strength as well as better fatigue stress rupture properties at elevated temperatures. The static strength of Inconel 718 is induced by particle strengthening effect of secondary precipitates and solid solution hardening. The major part of the strengthening at elevated temperatures is caused by the secondary precipitates γ' and γ'' [3-7].

SLM is a very complex process with a number of non-equilibrium phenomena depending on the process details. The final product fabricated by localized melting and solidification of gas atomized Inconel 718 powder is strongly influenced by process parameters like the laser power and the beam diameter, scanning parameters and, indeed, the starting material powder. Moreover, the thermal conductivity, temperature and the environmental conditions in the process chamber play an important role. The static performance of many SLM materials is found to be reasonably comparable in terms of the ultimate strength, yield strength and elongation to conventionally manufactured materials. By reason of the advantages of the SLM technology there is a strong tendency to apply it even where not only the static but also fatigue properties are decisive for reliable and long term operation. Due to the complex interaction of SLM process parameters, resulting microstructure and material properties, the generation of the needed fatigue design data is quite complicated because the fatigue behavior appears highly susceptible to of SLM process issues, such as porosity, build orientation, residual stress and surface condition [8-10]. Because the SLM fabrication route is increasingly applied to Inconel 718, its fatigue behavior and the fatigue crack propagation data are desirable for a more widespread use.

This study is aimed at the microstructural characterization of Inconel 718 manufactured by SLM and at the determination of long fatigue crack growth data. The crack growth behavior and the mechanism of crack tip interaction with the specific SLM microstructure during crack propagation are discussed.

EXPERIMENTAL ACTIVITY

Experimental methods

The base material for SLM process was in the form of atomized Inconel 718 powder with a granulometry in the range from 20 to 50 μm (Fig. 1). The Nickel-based superalloy Inconel 718 powder has the nominal chemical composition given in tab. 1 (corresponds to the Standard DIN NiCr19Fe19NbMo3).

Ni	Fe	Cr	Nb	Mo	Ti	Al
52.5	18.4	19.9	5.1	3.22	0.92	0.71

Table 1: Chemical composition in wt. %.

The specimens for fatigue crack growth testing were produced by SLM on a RENISHAW A250 machine schematically depicted in Fig. 2 [11]. This system features a vacuum chamber, which after low-pressure atmospheric evacuation allows the refill of the chamber with high purity argon gas. A soft blade evens out each fresh layer of powder material across the surface of the bed before consolidation by the laser. The machine is equipped with a fiber laser (wavelength λ = 1070 nm) with a maximum power of 200 W. All specimens were made at the full laser power. The modulated pulsed-laser moves in a raster fashion 50 μm point-to-point and with a point exposure time of 251 μs. The scanning speed was approximately 200 mm/s. The lateral separation between consecutive scan lines was set at 180 μm whereas the layer thickness was fixed at 50 μm. The selective layer-by-layer melting of the powder by the laser beam induces an inherent texture in the SLM material. Consequently, the parts have some degree of anisotropy.

Compact-tension (CT) specimens according to the geometry specified in ASTM E 647-08 were fabricated by the SLM process. The build direction was parallel to the crack propagation plane as shown in Fig. 3. A typical, as-produced Inconel 718 CT specimen is shown in Fig. 4. It is pointed out that the pin holes and the starter notch were obtained directly. The pin holes were then reamed to the final dimension and tolerance.

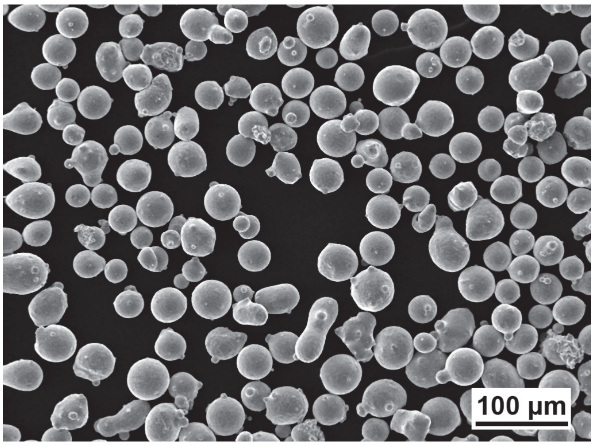

Figure 1: The range of powder sizes, SEM.

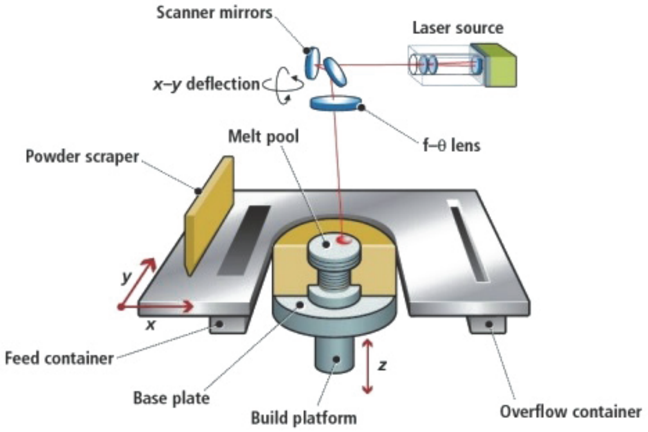

Figure 2: Scheme of a SLM machine [11].

Specimens for metallography were cut out from CT specimen halves after testing in such a way that the microstructure in the three main planes defined in Fig. 3 could be observed. Specimens were hot-pressed into Duroplast using CitoPress-1 device. Metallographic specimens were prepared using an automatic grinding and polishing system TegraPol-15. Grinding was conducted using SiC paper (220 grit) and fine sanding on the MD Largo discs with the addition of DiaProAlegro Largo emulsion. Polishing was conducted using MD Dac canvas with the addition of DiaProDac emulsion, followed by a final chemical polishing on the MD Chem polishing canvas with the addition of OP-S suspension.

The metallographic analysis was performed using light microscope Neophot 32 and Zeiss Axio Observer Z1M on metallographic specimens etched by Kalling's reagent (2 g of $CuCl_2$, 40 ml of HCl, 80 ml of methanol). The microstructure was observed at higher magnification in the scanning electron microscope (SEM) after re-polishing of used specimens for LM and etching by agent with composition 40 ml HNO_3 + 30 ml HF.

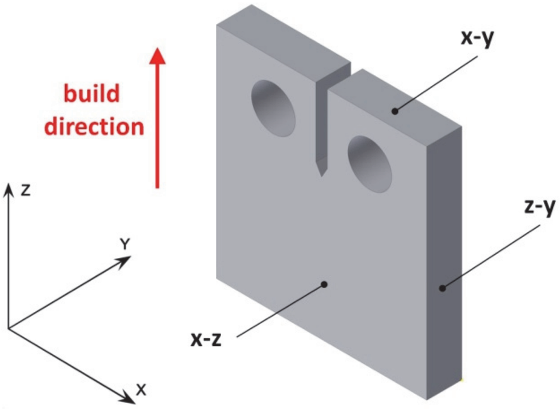

Figure 3: CT specimen orientation with respect to build direction.

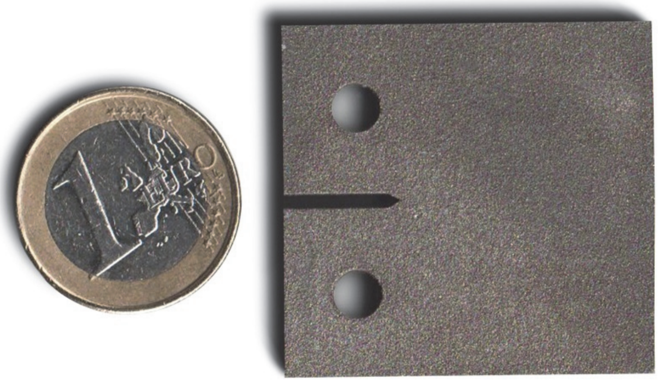

Figure 4: CT specimen made of SLM Inconel 718.

Vickers hardness measurement was performed using 250 HPO/AQ apparatus. The load of 98.1 N (10 kp) was applied for 10 s. Fracture surfaces were observed in a Tescan LYRA 3 XMU FEG/SEM microscope.

The fatigue crack growth (FCG) experiments were conducted on a Roell/Amsler HFP 5100 resonant testing machine in load control under load cycle asymmetry $R = P_{min}/P_{max} = 0.1$. The loading frequency was dependent on the crack length, i.e. on the stiffness of the cracked specimen and was in the interval from 80 to 60 Hz. Crack propagation measurement was performed at ambient laboratory conditions. The crack length was optically measured checking the two lateral sides of the specimen, which were mechanically polished. The resolution of determination of the crack tip position by means of CCD cameras with suitable optics was 0.01 mm. The measurement fulfilled the requirements of the ASTM E647-08 standard.

The fatigue growth tests were started at load amplitudes resulting in initiation of a fatigue crack from the starting chevron notch after some hundreds of thousand cycles. When the crack appeared on both lateral sides of the specimen the load amplitude shedding procedure fulfilling the load ratio condition R = 0.1 was applied to reach the crack growth rate of about 1 x 10^{-6} mm/cycle. Then the load amplitude was held constant and the practical determination of the crack growth rate was started after the crack grew through the area influenced by the load shedding procedure.

The lowest crack growth rates of the order of 1 x 10^{-7} mm/cycle in the threshold region were measured by load shedding method. The load was reduced in steps which were at the most of 10 % of the preceding value. As valid data were considered only those which were determined after the crack had grown through the corresponding cyclic plastic zone and when the average crack increment on both sides of the specimen was larger 0.1 - 0.2 mm.

RESULTS

Microstructure

As-fabricated CT specimens produced by SLM exhibit strong directionality of the microstructure. A three-dimensional cube (Fig. 5) shows the characteristic structure on section planes whose orientation with respect to the CT specimen is shown in Fig. 3. The z-axis coincides with the build direction; the x-y plane is parallel to the build plane. The scanning laser beam direction lies in x-y plane, which is perpendicular to the build direction. The fatigue crack in CT specimen propagated macroscopically in the x-z plane against the build direction.

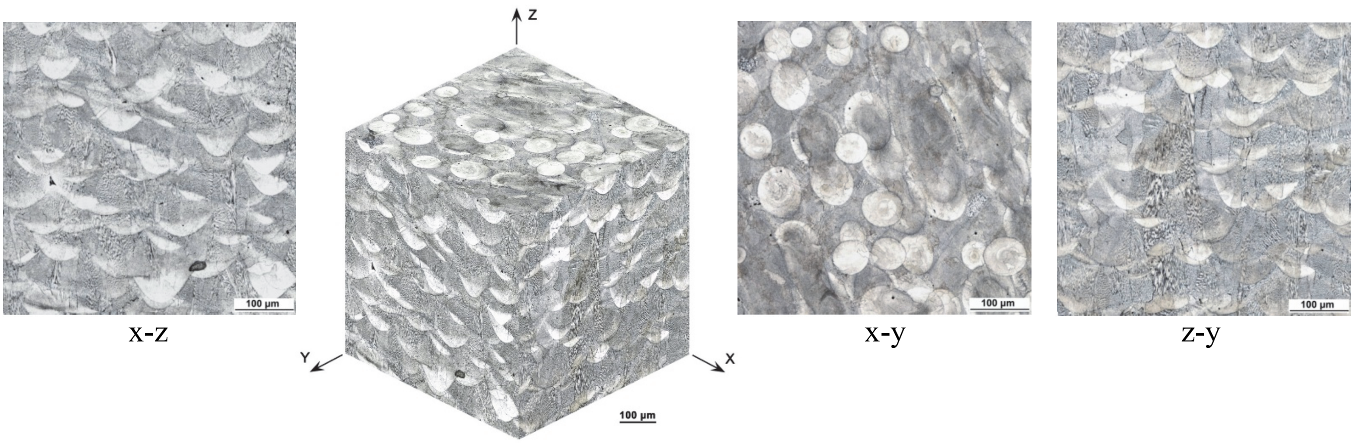

Figure 5: Layered structure of SLM Inconel 718, LM.

The micrographs taken at lower magnifications by light microscopy reveal the SLM process characteristics: line-by-line and then layer-by-layer building-up of the bulk (Fig. 5). In x-z and y-z planes the cut of melted tracks shows series of arcs produced by the laser energy distribution. The melt pools and layered structure appear as the result of laser beam alternating motion in x-y plane. Each next layer overlaps the previous melt pool tracks and due to heating influences the microstructure of the previous layer. All melted tracks are closely stacked to form a good metallurgical bonding between two neighboring layers. Defects in the form of small microshrinkages between the connected layers were found only rarely in the material. Similarly, small gas pores manifesting themselves as black round spots were observed only locally. The observed layer structure and melt pool tracks are typical features of the SLM production in various materials when the build strategy is of the type used in this study.

The melt pool width on metallographic section in x-z plane (yellow arrow in Fig. 6a) varies approximately from 50 to 100 μm. The average layer thickness is of about 40 μm. The white arrows in Fig. 6a, c indicate melt pool boundaries. Big columnar grains oriented in the build direction are present in the structure. They appear as dark and elongated columns (Fig. 6a) and are characterized by two different types of microstructure, which are shown at higher magnification in Fig. 6b, c. The microstructure corresponding to the region 1 (Fig. 6a) is formed by very small cuboidal particles of γ' precipitates in solid solution γ (Ni-Cr) fcc matrix (Fig. 6b). The intermetallic γ' precipitates of Ni_3(Al, Ti, Nb) composition have also the fcc structure. Fig. 6c shows a detail of the elongated (microdendritic) structure in region 2 (Fig. 6a). This structure is a result of grain growth at very high cooling rates. Long columnar grains develop preferably in the direction parallel to the build direction. The different microstructures are shown at higher magnification on SEM images in Fig. 6d, e. The boundaries of columnar grains, which are not well revealed by LM, were observed by SEM (Fig. 6d). Examples of cuboidal and elongated microstructure can be seen in Fig. 6d, e.

a) columnar grains with two different structure features, LM

b) cuboidal particles (precipitates) in region 1, LM

c) elongated structure in region 2, LM

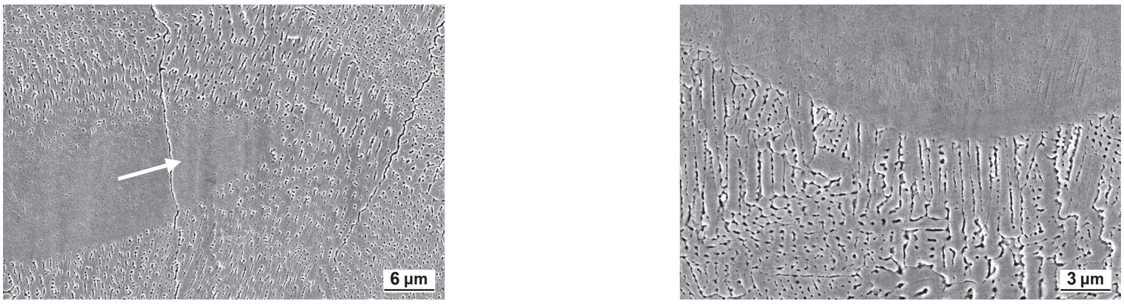

d) detail of columnar grain with boundaries, SEM

e) elongated particles and area with cuboidal particles, SEM

Figure 6: Structure of SLM Icnonel 718 in x-z plane.

Microstructure characteristics in the x-y plane, i.e. parallel to the build plane, are shown in Fig. 7. The sections of melt pools depicted in x-z and z-y planes as arcs appear as circles in the x-y plane (Fig. 7a). The microstructure within the circles is characterized by very small polyhedral grains of about 20 μm in size. Fine γ′ cuboidal particles are typical microstructural units within the melt pools, Fig. 7b. An example of non-melted particle with dendritic structure (inside circle) can be seen in Fig. 7d. The dendritic structure of powder remained unchanged because this particle was obviously not completely melted (Fig. 7d).

The size of γ′ particles in the form of cubes in the melt pool areas is much smaller than in the columnar grains. Their size is smaller than 1 μm (Fig. 7e). The elongated structure in the area marked as 2 in the section x-z appears as ellipsoidal elongated particles in x-y metallographic section (Fig. 6e, Fig. 7c, f).

The Vickers hardness does not depend on the plane orientation with respect to the build direction. The hardness measured on the x-y plane is HV10 = 330 ± 11 while on the z-y plane HV10 = 338 ± 11. The average value of Vickers hardness corresponds to the Rockwell hardness 34 HRC, which is a typical value for precipitation hardened Inconel 718 manufactured by conventional techniques [11].

Fatigue crack growth behavior

The experimentally determined dependence of the crack growth rate da/dN on the stress intensity factor amplitude $K_a = (K_{max}-K_{min})/2$ is shown in Fig. 8. It can be seen that a linear dependence in a log-log plot well approximates the crack growth rate data in the interval 1 x 10^{-6} to 1 x 10^{-4} mm/cycle, i.e.in the Paris equation:

$$da/dN = 2.25 \times 10^{-7} K_a^{2.31}. \tag{1}$$

The data in Fig. 8 show that the lowest value of the stress intensity factor amplitude K_a at which the crack growth rate was reliably measurable for R = 0.1 is 1.5 MPam$^{1/2}$. This value can be considered the threshold value of the stress intensity factor amplitude or K_{ath}.

a) polyhedral grains in circles and in columnar grains, LM

b) detail of polyhedral grains in the circle, LM

c) cuboidal and ellipsoidal particles, LM

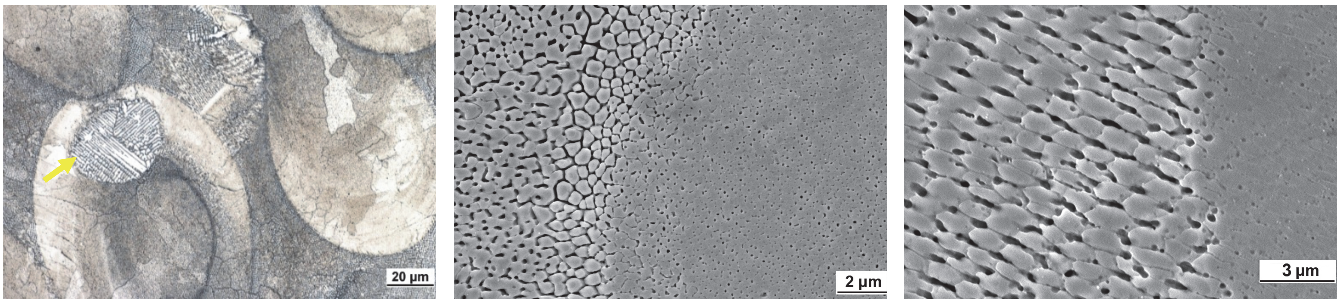

d) non melted powder particle

e) cuboidal particles, SEM

f) elongated particles, SEM

Figure 7: Structural details in the x-y plane

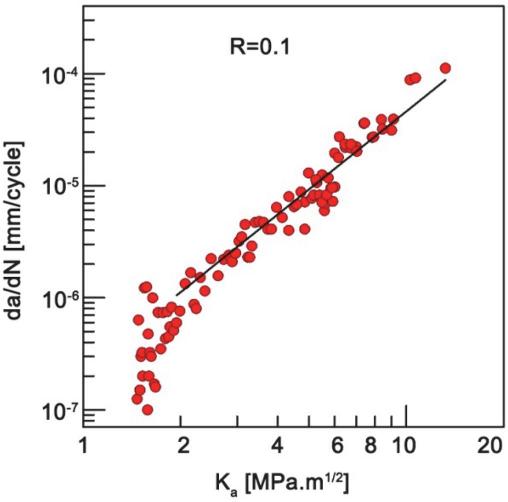

Figure 8: Fatigue crack growth data for SLM Inconel 718 alloy

Fractography

The local crack growth rate is influenced by the local microstructure and the level of applied stress intensity factor. Examples of characteristic fracture surfaces, as observed by SEM, are presented in Figs. 9 and 10.

The fatigue fracture surface corresponding to the crack growth rate of 8 x 10^{-7} mm/cycle and the stress intensity factor amplitude K_a = 2.0 MPa $m^{1/2}$ (i.e. near the threshold) is shown in Fig. 9 (note that the macroscopic crack propagation direction is from top to bottom). The macroscopic plane of the fracture surface is parallel to the building direction of SLM process. The crack propagates in a transgranular manner. The fracture surface is characterized by many parallel secondary cracks, which are often markedly opened. The secondary cracks are indicated in Fig. 9a with arrows. The average distance of the parallel secondary cracks is of about 0.5 µm, which is a value nearly three orders of magnitude larger than the average crack increment at the corresponding crack growth rate. The variability of the fracture surface in the near threshold region is demonstrated by Fig. 9b, where the secondary cracks are rarely observed. The fracture surface is again transgranular without any specific fractographic features, see region A. Region B in the figure is characteristic by elongated areas covered by fine slip lines. No secondary cracks are visible here. Arrows in Fig. 9 indicate the local direction of the crack growth. Locally it differs a lot from the macroscopic direction.

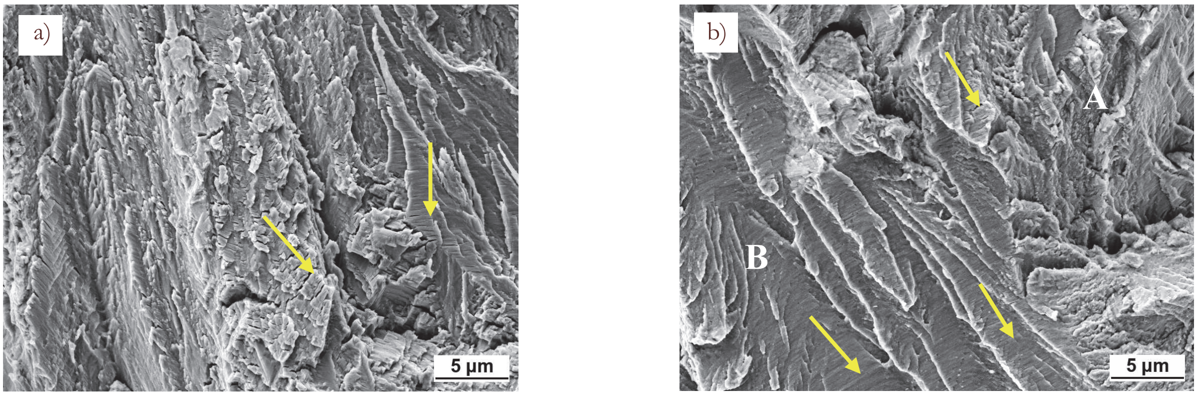

Figure 9: Fracture surface corresponding to the average crack rate 8 x 10^{-7} mm/cycle

The fracture surface corresponding to the crack propagation in Paris region is shown in Fig. 10. The surface was created by the crack propagating at the growth rate of 1 x 10^{-5} mm/cycle. The appearance is very similar to that shown in Fig. 9. In comparison to the threshold region some of the secondary cracks are longer and more open. The traces of slip lines are also visible, see arrow in Fig. 10b.

Well-developed striations appear at high crack growth rates reaching 1 x 10^{-4} mm/cycle. An example is shown in Fig. 11. The striation distance roughly corresponds to the macroscopic crack growth rate.

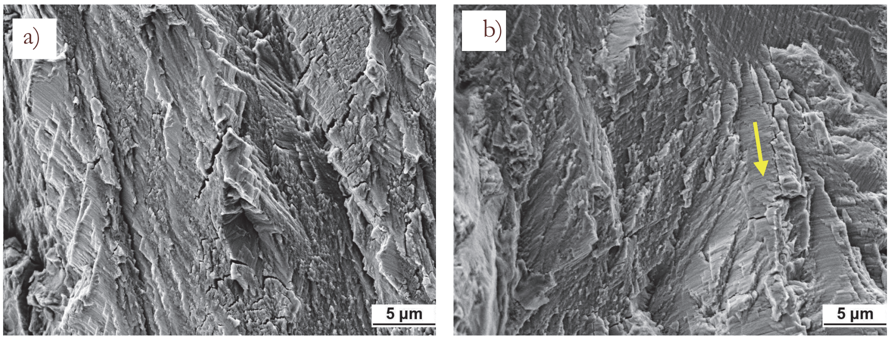

Figure 10: Fracture surface corresponding to the average crack rate 1 x 10^{-5} mm/cycle.

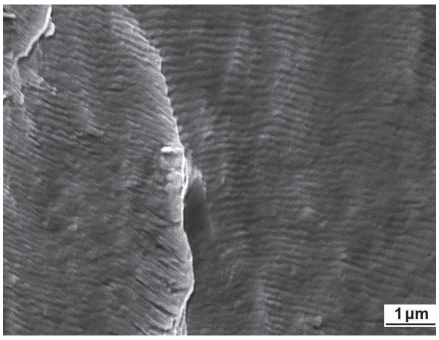

Figure 11: Fracture surface corresponding to the crack growth rate 1 x 10^{-4} mm/cycle.

Fatigue fracture profiles

The fracture profiles as observed by LM on polished and etched sections in y-z plane direction and perpendicular to the fracture surface are shown in Fig. 12. The crack growth direction was from the right to the left (arrow in Fig. 12a). The fatigue crack propagates in the threshold region in a transgranular way and is obviously not influenced by the specific SLM microstructure. The fracture profile view corresponding to K_a = 1.6 MPam$^{1/2}$ and da/dN ~ 10^{-7} mm/cycle is flat with local small sharp asperities (Fig. 12a). Secondary cracks emanating from the main crack do not have any visible relation to the microstructure. Fig. 12b shows the crack profile typical for the Paris region. The only difference is in the roughness of the fracture profile, which is higher when compared to the roughness of the fracture profile in Fig. 12a. The crack propagation remains transgranular.

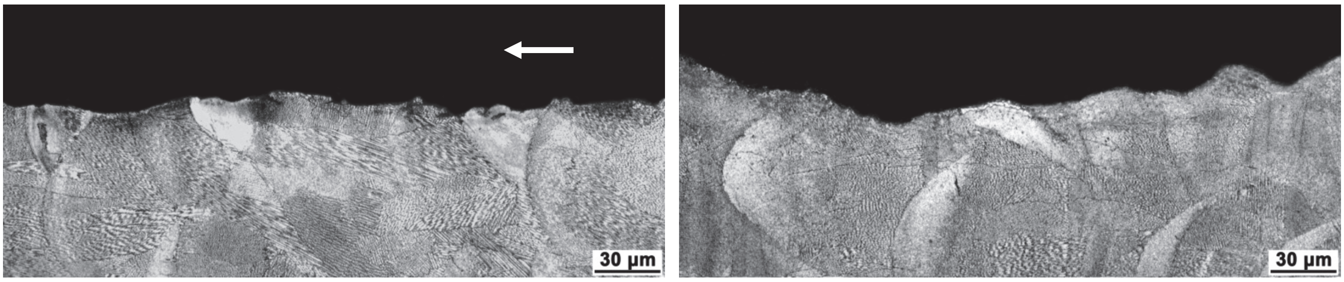

a) K_a = 1.6 MPam$^{1/2}$, da/dN ~ 10^{-7} mm/cycle. b) K_a = 5.0 MPam$^{1/2}$, da/dN ~ 10^{-5} mm/cycle.

Figure 12: Fracture profiles of fatigue crack path, LM

Discussion

SLM Inconel 718 in contrast to conventionally manufactured alloy exhibits strong features of local directional solidification. The SLM CT specimens exhibit a columnar microstructure [12] which was found and analyzed also in this paper (Fig. 5, Fig. 6). Microstructure of parallel elongated fine columns (Fig. 6a, c) was characterized in [13, 14] as a fine columnar microdendritic structure. The sections of fine columns by a metallographic plane inclined at a high angle to their long axis have an ellipsoidal shape (Fig. 6c, Fig. 7f) whose dimensions are obviously dependent on the mutual orientation of columns and the metallographic section. The cuboidal structure corresponds to the γ′ phase (precipitates $Ni_3(Al, Ti)$. The preferred formation of γ′ rather than γ″ precipitation has been shown to be dependent on Ti + Al/Nb ratio [4, 5]. Cozar et al. [5] conclude that if the Ti + Al/Nb ratio is above a critical value (from 0.9 to 1) the γ′ precipitates formation prevails over the γ″ formation. That ratio for the present material is 1.26 that is substantially higher than the critical range. In some cases special cube-shaped γ′ particles coated with a γ″ shell were identified. This effect is related to very slow coarsening rate [5].

The propagation of long cracks in conventionally manufactured Inconel 718 at ambient and high temperatures was studied intensively in the past [15-17], because this alloy is often used for fabrication of components exposed to long term cyclic loading at high temperatures. Also the mechanism of the crack growth was a subject of investigation. The threshold values for propagation of long cracks have been shown to be dependent on temperature and microstructure. Recently Yamada et al. [18] presented a detailed study on the effect of crack closure on the crack growth. Their measurements indicate high threshold at R = 0.1, which is attributed to anticipated crack closure in the loading cycle. The near-threshold FCG data at R = 0.7, on the other hand, are apparently crack closure free.

The fatigue crack growth curves, particularly in the threshold region, were shown to be strongly dependent on the chemical composition. The content of boron ranging from 12 to 100 ppm decreases the crack growth rate substantially [19]. The loading with the stress intensity factor amplitude K_a = 5.0 MPam$^{1/2}$ in the case of the lowest B concentration results in identical crack growth rate of 1 x 10^{-6} mm/cycle as in material with highest B content loaded at K_a = 7.2 MPam$^{1/2}$ [19].

Contrary to the case of conventionally manufactured alloy the knowledge on the mechanical properties of SLM Inconel 718 is limited. As regards the tensile properties, they are comparable to those of wrought material [20]. Influence of processing parameters, like atmosphere in the building chamber, was reported, but these effects seem to be weak. On the other hand, the comparison of the fatigue crack growth curves of wrought and SLM manufactured alloy shows substantial differences, Fig. 13.

The data determined in this study are compared with the measurements by Clavel and Pineau [15]. Both crack growth experiments were performed for identical loading asymmetry R = 0.1 on similar CT specimens. The crack growth rates above 5 x 10^{-5} mm/cycle in both materials can be considered as identical within the data scatter band. Strong difference, however, appears in the near-threshold region. The resistance of the SLM material against crack growth is substantially lower. Similar conclusions can be made when data for SLM material are compared with result by Yuen et al. [17]. The threshold stress intensity factor amplitude K_{ath} of SLM material based on the crack growth rate 1 x 10^{-7} mm/cycle makes only 25 % of the value determined in [15] and 35 % of value found in [17].

The threshold value in conventionally manufactured Inconel has been shown to depend on the boron content. In our case the boron content is higher than 100 ppm. It means that the threshold value determined in this study for SLM material should be compared with the value of about K_{ath} ~ 6 MPam$^{1/2}$ [19]. This comparison again indicates the disadvantage of SLM produced material as regards the resistance to the growth of long cracks.

The explanation of the lower threshold values of SLM alloy can be substantiated by the different microstructure. The SLM alloy exhibits very fine grain. The grain size is of about 10 µm, whereas the alloy studied by Clavel and Pineau [15] had the grain size 30 µm. This finding is consistent with general trend of decreasing threshold with decreasing grain size. The fracture profile presented in Fig. 12a shows that the fatigue crack propagates in the threshold region through the microstructure without any specific interference with the structural features, like grain boundaries. No correspondence of the fatigue crack paths and the melt pool tracks or particular building layers can be identified. The crack propagation is of transgranular manner, which is well documented in Figs. 9 and 10. The fracture surface is very similar to that reported for conventionally manufactured alloy [15].

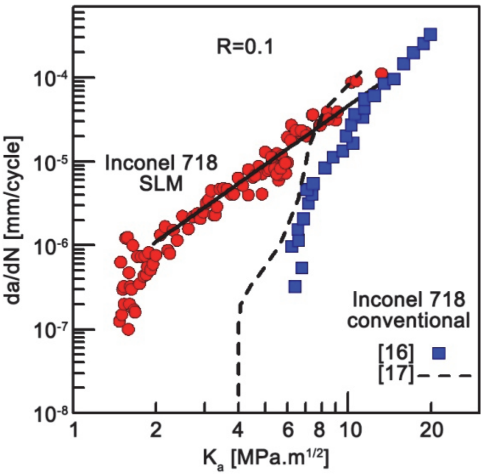

Figure 13: Comparison of crack growth in Inconel 718 manufactured conventionally and by SLM.

The mechanism of the crack propagation is based on the planar cyclic slip in the region ahead the main crack tip. The cyclic slip is localized on parallel slip planes. The cycling leads to gradual damage of suitably oriented slip bands and formation of microcracks. Some of them are significantly opened. The main crack propagates by their linking or by rupture of areas in which the slip activity due to inconvenient orientation was weak. This mechanism is similar to that known from conventionally manufactured alloy [20]. The crack path is entirely transgranular. The slip activity in suitably oriented grains manifests itself by parallel slip lines visible on the fracture surface. The mechanism of the crack growth in the near-threshold region and in the Paris region is basically the same. Only the volume of the material at the main crack tip which is cyclically deformed is larger, which manifests itself by larger and more opened microcracks.

At crack growth rates reaching 1 x 10^{-4} mm/cycle formation of striations was observed, Fig. 11. This witness for the change of mechanism of the fatigue crack growth to ductile at high K_a values. The plastic blunting model of crack growth can be considered as appropriate for crack advance description at high crack growth rates. Similar behavior was reported for conventionally manufactured alloy [20]. Simultaneously, in this crack growth region the da/dN vs. K_a curves of both alloys are identical.

CONCLUSIONS

1. The propagation of long cracks at RT and at stress ratio R = 0.1 in Inconel 718 manufactured by selective laser melting can be well described by the equation $da/dN = 2.25 \times 10^{-7} K_a^{2.31}$. The threshold value of the stress intensity factor amplitude is $K_{ath} = 1.5$ MPa m$^{1/2}$. The SLM alloy is less resistant to the growth of long cracks in the near-threshold region than the conventionally manufactured alloy. For the loading with the stress intensity factor amplitude exceeding 10 MPa m$^{1/2}$ the crack growth resistance of SLM and wrought alloys is identical.
2. Fatigue crack growth occurs in transgranular mode. The cyclic plasticity is localized into parallel slip bands. The mechanism of the crack growth at threshold and in Paris region consists in the formation of microcracks ahead of the main crack. The main crack grows by their linking. At high crack growth rates the mechanism of crack growth changes and the occurrence of striations was observed. On the microscopic level the local direction of crack growth is dependent on the grain orientation.
3. The microstructure of SLM Inconel 718 exhibits specific features related to the building process. The melt pools are typical by fine grained microstructure and very small precipitates. The remaining volume is composed of coarse columnar grains having often elongated microstructure. The defects in the form of small voids and cavities are rare.

ACKNOWLEDGEMENTS

The authors wish to acknowledge the company Protoservice srl., Fornovo Taro, Italy for providing the Inconel 718 specimens produced by SLM and the research was supported by project VEGA grant No. 1/0685/2015.

REFERENCES

[1] Kruth, J. P., Levy, G., Klocke, F., Childs, T. H. C., Consolidation phenomena in laser and powder-bed based layered manufacturing, CIRP Ann. Manuf. Technol., 56 (2007) 730-759.

[2] Yadroitsev, I., Thivillon, L., Bertrand, P., Smurov, I., Strategy of manufacturing components with designed internal structure by selective laser melting of metallic powder, Appl. Surf. Sci, 254 (2007) 980-983.

[3] Zhang, H. Y., Zhang, S. H., Cheng, M., Li, Z. X., Deformation characteristics of δ phase in the delta-processed Inconel 718 alloy, Materials Characterization, 61 (2010) 49-53.

[4] Kirman, I., Warrington, O. H., Precipitation in nickel-based alloys containing both niobium and titanium, J. Inst. Metals, 99 (1971) 197-202.

[5] Cozar, R., Pineau, A., Morphology of γ' and γ" precipitates an thermal stability of Inconel 718 type alloys, Metall. Trans, 4 (1973) 47-59.

[6] Sundararaman, M., Mukhopadhyay, P., Banerjee, S., Some aspects of the precipitation of metastable intermetallic phases in Inconel 718, Metall. Trans, 23A (1992) 2015-2028.

[7] Durand-Charre, M., Davidson, J. H., The Microstructure of superalloys, Gordon and Breach Science Publ., Amsterdam, (1997) 124.

[8] Gu, D., Shen, Y., Balling phenomena in direct laser sintering of stainless steel powder: Metallurgical mechanisms and control methods, Materials and Design, 30 (2009) 2903-2910.

[9] Janaki Ram G. D., Venugopal Reddy, A., Prasad Rao, K., Reddy, G. M., Sarin Sundar, J. K., Journal of Materials Processing Technology, 167 (2005) 73-82.

[10] Murr, L. E., et al., Microstructural architecture, microstructures, and mechanical properties for a nickel base superalloy fabricated by electron beam melting, Metall. Trans A, 42A (2011) 3491-3508.

[11] Kruth, J. P., Badrossamay, M., Yasa, E., Deckers, J., Thijs, L., Van Humbeeck, J., Part and material properties in selective laser melting of metals. 16th International Symposium on Electromachining (ISEM), Shanghai, China, (2010).

[12] Amato K. N., et al., Microstructures and mechanical behavior of Inconel 718 fabricated by selective laser melting, Acta Mater., 60 (2012) 2229-2239.

[13] Jia, Q., Gu, D., Selective laser melting additive manufacturing of Inconel 718 superalloy parts: Densification, microstructure and properties, J.Alloys Comp, 585 (2014) 713-721.

[14] Wang, Z., Guan, K., Gao, M., Li, X., Chen, X., Zeng, X., The microstructure and mechanical properties of deposited-IN718 by selective laser melting, J.Alloys Comp, 513 (2012) 518- 523.

[15] Clavel, M., Pineau, A., Frequency and wave-form effects on the fatigue crack growth behavior of alloy 718 at 298 and 823 K, Metall. Trans A, 9A (1978) 471-480.

[16] Clavel, M., Pineau, A., Fatigue behavior of two nickel-base alloys. I. Experimental results on low cycle fatigue, fatigue crack propagation and substructures. Mat. Sci. Eng A, 55 (1982) 157-171.

[17] Yuen, L. J., Roy, P., Nix, W. D., Effect of oxidation kinetics on the near threshold fatigue crack growth behavior of a nickel base superalloy, Metall. Trans A, 15A (1984) 1769-1775.

[18] Yamada, Y., Newman Jr., J. C., Crack closure under high load-ratio conditions for Inconel-718 near threshold behavior, Eng. Fract. Mech., 76 (2009) 209-220.

[19] Xiao, L., et al., Effect of boron on fatigue crack growth behavior in superalloy IN 718 at RT and 650 °C, Mat. Sci. Eng. A, 428 (2006) 1-11.

[20] Andersson, H., Persson, C., In-situ SEM study of fatigue crack growth behaviour in IN718, Int. J. Fatigue, 26 (2004) 211-219.